Charge state and stopping dynamics of fast heavy ions in dense matter

O. N. Rosmej,* A. Blazevic, S. Korostiy, and R. Bock
Gesellschaft für Schwerionenforschung mbH, Plasma Physik, Darmstadt, Germany

D. H. H. Hoffmann
Gesellschaft für Schwerionenforschung mbH, Plasma Physik, Darmstadt, Germany and Technical University, Darmstadt, Germany

S. A. Pikuz, Jr., V. P. Efremov, and V. E. Fortov
Institute for High Energy Density, Russian Academy of Sciences, Moscow, Russia

A. Fertman and T. Mutin
Institute of Experimental and Theoretical Physics, Moscow, Russia

T. A. Pikuz and A. Ya. Faenov
Multicharged Ions Spectra Data Center of VNIIFTRI, Mendeleevo, Russia

K-shell radiation of fast heavy ions penetrating solid matter was used to analyze the stopping dynamics of ions over more than 80% of the stopping path. The most important advantage of this method is that the data is obtained with a high spatial resolution directly from the interaction volume. In experiments 11.4 MeV/u Ca projectile were slowed down in solid quartz and low-density SiO_2 aerogel targets. Characteristic projectile and target spectra in the photon energy range of 1.5–4 keV were registered by means of spherically bent crystal spectrometers with high spectral and spatial resolution in the direction of the ion beam propagation. K-shell spectra of heavy ions induced by close collisions with target atoms provided information about the projectile charge state and velocity dynamics. The line intensity distribution of the K-shell transitions arising from ions with different ion charges represents the charge state distribution along the ion beam track. The variation of the line Doppler shift due to the ion deceleration in the target material was used to determine the ion velocity dynamics. The spectroscopic analysis of the stopping process was complemented by measurements of the energy loss and ion charge state distribution after the ion beam emerged from the target using a standard time-of-flight method and magnet spectrometer.

PACS number(s): 34.50.Bw, 32.30.Rj, 39.30.+w

I. INTRODUCTION

One of the main questions of the ion stopping theory is the relationship between the charge and velocity of the projectile ion traversing matter. The Bohr-Bethe-Bloch formalism [1] describes generally a strong dependence of the medium stopping power on the ion velocity and the charge state. In this concept, the charge state dependence is usually taken into account by the effective charge Z_{eff} introduced by Northcliffe [2] as the square root of the ratio of the measured stopping cross section of an ion with a nuclear charge Z to that of a proton having the same velocity.

However, practically no experimental information is available on the relationship between the actual ion charge and effective charge Z_{eff}. Sigmund emphasizes in [3]: "While there is general agreement that the effective charge cannot be identical with the ion charge measured on emergence from a foil, the relation between the two and the dominating origin of the difference is far from clear."

Due to the absence of the analytical expression for the ion charge as a function of the speed, empirical and semiempir-ical relations are employed based on the experimental data of the ion charge state distribution after the beam emerging the target [4–7]. The discovered difference in the ion stopping power and charge distribution of the ions penetrating solid and gaseous matter [8,9] opened the discussion about the equivalency of the ion charge state distribution measured "outside" the stopping media to that "inside." There is still no experimental answer on the question whether the projectile charge alters at the target-vacuum boundary due to collisionless processes.

The second very important question which gets more and more actuality due to the possibility in the close future of using heavy ion beams for plasma generation [10,11] is the dependence of this relationship on the properties of the stopping media. Ion beams with two-order-of-magnitude higher intensities than available now can be applied for matter heating in warm dense matter and thermonuclear fusion scenarios [12,13]. In both cases, the intense ion beam irradiates first a cold solid or porous target. During the interaction time, the heated target material undergoes subsequent phase transitions into liquid, gaseous, and plasma states [13]. Variations of the target material properties such as density and degree of ionization can influence the ion stopping cross sections significantly and change the relation between the ion charge and the ion energy [14–16].

---

*Corresponding author. Electronic address: o.rosmej@gsi.de

The standard concept considering the ion penetrating stopping media as a point charge is not able to describe these effects. Today it is obvious that the detailed knowledge of the projectile-bound electron dynamics during the stopping process is of great importance [17–19]. Maynard *et al.* in [20] provided the theoretical description of the evolution of the projectile ion average configurations during its interaction with dense (ionized) target material. For the simulations of the ion-atom interactions a collisional-radiative model was used. The calculations exhibit a significant influence of atomic collisions on the energy loss process.

The properties of the stopping media influence the structure of the projectile bound electrons and therefore the effective screening of the Coulomb field of the nucleus. The concept of the projectile charge related to the stopping cross sections can exist only in connection with the properties of the stopping matter. However in many experiments [21], a projectile charge state distribution is usually measured after the ions left the interaction volume and therefore, after a possible change of its charge and electron distribution over exited states due to collisionless processes like the Auger effect and spontaneous radiative decay to the projectile ground state.

In the present experiments we made use of *K*-shell radiative transitions of energetic ions penetrating solid targets for determination of the projectile charge state and velocity along the ion beam trajectory during the ion stopping process. The spectroscopic analysis of the stopping process was complemented by measurements of the energy loss and ion charge state distribution after the ion beam emerged from the target using standard time-of-flight method and a magnet spectrometer.

II. EXPERIMENTAL METHOD

The characteristic projectile radiation induced by collisions with target atoms proceeds predominantly via resonant radiative transitions—allowed dipole transitions into the ion ground state. Their photon energies for elements with a nuclear charge $Z_{nuc}=6$–30 cover wide vuv and x-ray regions depending upon the amount of bound electrons of the projectile (ion charge state).

The energies of *K*-shell radiative transitions vary slightly with the ion charge due to shielding effects produced by bound projectile electrons, and belong to the x-ray region. Such kind of radiation can appear due to the ionization of the *K*-shell electron and a subsequent radiative transition into this vacancy. This enables us to observe all possible projectile charge states by means of the same x-ray detector and to avoid calibration problems due to observation of the ion charge state dynamics caused by ionization and recombination processes.

K-shell ionization cross sections depend strongly on the projectile ion energy and only slightly on the projectile charge state. Figure 1 shows the charge and energy dependence of *K*-shell ionization cross sections of Ca^{q+} ions ($q=15$–19) colliding with SiO$_2$ molecules. The cross sections are calculated by the LOSS code described in [22] using the additive rule for the SiO$_2$ target, i.e., presenting SiO$_2$
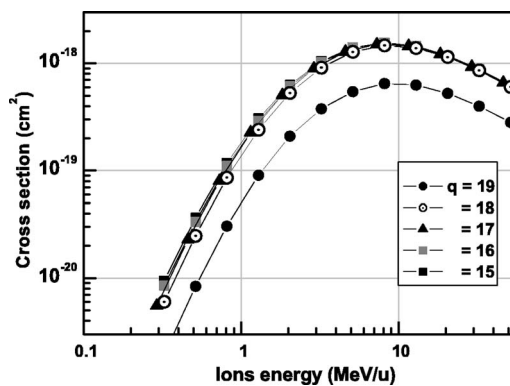

FIG. 1. *K*-shell ionization cross sections of Ca^{q+} ions ($q=15$–19) colliding with SiO$_2$ molecules as a function of the ion energy, calculated by the LOSS code [22].

molecule as a sum of one silicon atom and two oxygen atoms. As is seen, all cross sections are peaked around 8 MeV/u and have only a weak dependence on the ion charge because *K*-shell electrons move in the nuclear field slightly shielded by other electrons. The difference of about a factor of 2 between the curve for $q=19$ and curves for $q=15$–18 arises because Ca^{19+} has only one 1s electron.

In experiments we observed prominent *K*-shell transitions Ly$_\alpha$(1s-2p) and He$_\alpha$(1s^2-1s2p $^1P_1$) and their *K*α satellites $1s^2ml^k$-$1s2pml^k$ (here $m=2,3…$ is the principal quantum number), $l=0,…m-1$ is the orbital momentum and k is the amount of spectator electrons on the ml shell. The relative line intensities of these satellites reflect the charge state distribution of the ions.

The velocity of ions moving with one tenth of the light speed was analyzed using the Doppler effect. The Doppler line shift reduction (DSR) of the projectile *K*-shell radiation due to the ion deceleration measured with a high spatial resolution was applied for these purposes.

Thus the method provides the most important for the stopping theory information—the dynamical relationship between the ion charge and velocity along the ion trajectory. This information is obtained directly from the interaction volume due to high x-ray transmission coefficients of the media used.

III. EXPERIMENTAL SETUP

Experiments on the interaction of heavy ion beams with matter were carried out at the linear accelerator UNILAC at GSI-Darmstadt. The ^{48}Ca^{6+} projectile ions with initial energies of 11.4 MeV/u were slowed down in quartz or porous SiO$_2$ aerogels. The experimental objective was to receive spatially resolved information on the projectile ion charge and velocity dynamics in solids. The principal experimental scheme is shown in Fig. 2.

The Ca ion beam was delivered to the target chamber evacuated to 5×10^{-6} mbar with a typical focusing spot dimension on the target of 1–2 mm. The pulsed ion beam current was between 0.2 and 0.5 μA. After emerging from the target, the ion beam energy was determined using the time-of-flight method, and the ion charge state distribution was
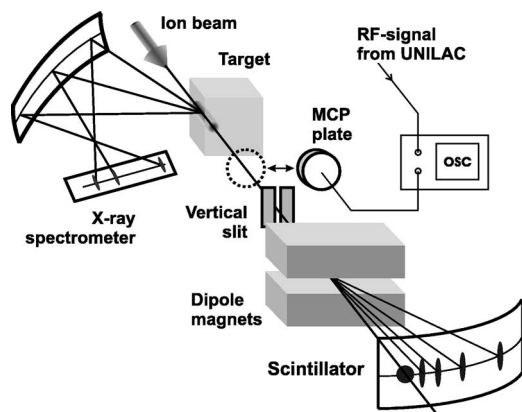
FIG. 2. Experimental setup for the measurements of the energy loss and charge state distribution of the ion beam by methods of x-ray spectroscopy, magnet spectroscopy and time-of-flight used simultaneously.

analyzed by means of the magnetic spectrometer. Measurements are described in detail in the Sec. IV. Associated K-shell radiation caused by inelastic collisions of heavy ions penetrating solid targets was measured with a high spectral and spatial resolution provided along the ion beam track.

K-shell x-ray spectra in the photon energy range of 1.5–4 keV were observed with a spatial resolution by mean of focusing crystal spectrometers (FSSR) [23]. The main principles of the spectral registration are shown in Fig. 3. For specific geometrical conditions, FSSR spectrometers allow combining Bragg reflection properties of the crystal lattice with focusing properties of the reflecting spherical surface.

The characteristic radiation of projectile ions and target atoms coming from the interaction region onto the spherically bent crystal (see Fig. 3) is reflected in the plane of dispersion, the so-called Rowland circle, according to the Bragg crystal x-ray diffraction law: $m\lambda = 2d_m\sin\Theta$. Here λ is the wavelength, m is the reflection order, d_m is the interplanar distance of the crystal for the mth order of reflection, and Θ is the Bragg angle for the central wavelength.

The spectrometer is able to provide spatially resolved (up to 2–5 μm) distribution of the x-ray emission in the direction perpendicular to the plane of the dispersion. In accordance with spherical mirror optics, the length of the spectral lines at the detector (x-ray film) is a magnified image of the
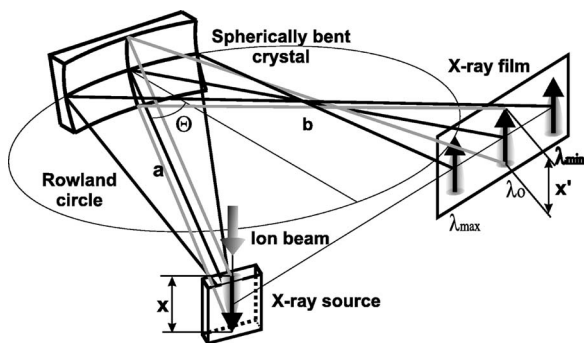

FIG. 3. Scheme of principles of x–ray focusing spectrometer with spatial resolution based on spherically bent crystal.

ion beam stopping path (see Fig. 3). Due to the focusing properties of the spherical crystal surface, FSSR is characterized by a very high luminosity and a large field of view together with very high spectral and spatial resolutions.

In experiments spatially resolved K-shell spectra of Ca projectile ions as well as K-shell spectra of the ionized stopping media were recorded. As dispersive elements, spherically bent mica and quartz crystals with radii of curvature R=150 mm and apertures of 15×50 mm^2 were used. The spectral resolution achieved in experiment was $\lambda/\Delta\lambda=3000$–5000; the spatial resolution was up to 30–70 μm.

Spatially resolved spectra were observed in the direction of ion beam propagation at 80° and 90° to the ion beam axis. Radiation was recorded using DEF-5 x-ray films which have a maximum of sensitivity in the photon energy range of 1–10 kV [24]. The exposure time needed to accumulate the x-ray signal was typically 2–5 h. It corresponds to a projectile ion fluence of about 10^{13} ion/cm^2 (for more details see [25]).

The main obstacle for a spatially resolved analysis of the ion stopping process in solids is a very short stopping length of 10 MeV/u projectile ions—up to 100 μm. In our experiments silica aerogels of 0.02–0.1 g/cm^3 mean densities were used as a target material providing the increase of the ion stopping length of 20–100 times in comparison with solid quartz. Silica aerogel is a transparent porous material. Its structure is formed by chains of colloidal SiO$_2$ beads of 3 nm in diameter. The chains build a three-dimensional open cell structure, like a sponge, with pores of 30–50 nm. The aerogel foam structure withstands temperatures up to 750 °C without damage. Because of the open cell structure, it can be evacuated [26,27].

The nanometer uniform aerogel structure provides a continuously expanded interaction volume with small spatial gradients. The wide variety of aerogel mean densities (0.02–0.5 g/cm^3) allows stretching the ion stopping length and reaching a high spatial resolution of the ion radiation dynamics. The pore structure will not influence the projectile charge state distribution due to the time of flight of the ion inside the pore in vacuum is shorter than the time scale of the radiative and Auger processes, which lead to the collisionless relaxation of the projectile excited states. The important advantage of this material is the high transparency for x-rays. In contrast to the 100-μm-thick piece of solid quartz which fully absorbs x-ray radiation of 1.5 keV photon energy, the transmission coefficient of the aerogel sample with 100 times lower density and the same thickness absorbs only 20% on that energy.

IV. EXPERIMENTAL RESULTS AND DISCUSSION

A. Measurements of the projectile energy and charge state distribution after penetration of solid and foam targets

To investigate the possible influence of the aerogel porous nanostructure on the ion stopping process, the energy loss and charge state distribution of the 11.4 MeV/u Ca ion beam interacting with Al foils and aerogel targets with approximately the same linear densities ρx were measured and ana-

TABLE I. Energy losses of 11.4 MeV/u Ca ions in SiO$_2$ aerogel and Al targets.

Target	Density (g/cm^3)	Linear density (mg/cm^2)	Energy loss (MeV/u)	
			Experiment	SRIM2003.26
Al		6.9	1.572	1.558
Al		12	2.882	2.812
Al		13.81	3.141	3.283
Al		16.98	4.17	4.15
Aerogel	0.023	7.015	1.692	1.77
Aerogel	0.019	12.0	3.061	3.16
Aerogel	0.048	13.6	3.384	3.635

FIG. 4. The profile of the ^{48}Ca beam charge state distribution after analyzing magnet: gray line, Ca charge state distribution after passing through the Al foil with a linear density of 13.8 mg/cm^2; black line, Ca charge state distribution after penetration of the 0.048 g/cm^3 aerogel target with a linear density of 13.6 mg/cm^2.

lyzed. The experimental scheme is presented in Fig. 2.

For energy loss measurements a time-of-flight (TOF) method was used. A stop detector consisting mainly of a micro sphere plate with a rise time of 150 ps was placed at the end of the 473 cm long time-of-flight path after the target. The 50 Ω geometry of the anode provides an optimum transmission of the fast signals. This method is based on the strongly resonant ion beam accelerating in the RFQ LINAC which leads to a well-defined phase correlation between the beam microstructure and the accelerating rf voltage structure ($\sim$36 MHz sine wave) at any point along the beam line including the target position and stop detector position. The stop detector signal and the UNILAC rf signal were recorded simultaneously using a two-channel digital oscilloscope (sample rate 2.5 GS/s). The phase correlation between the ion beam microbunches and rf-signal peaks measured without a target served as a time reference point. When the target is placed in the way of the ion beam, a phase shift of the beam microstructure relative to the rf signal occurs due to the ion energy loss on stopping medium. Together with an accurately measured target-detector distance (TOF distance) this shift gives a difference between the initial ion velocity and the velocity after the beam passed through the target. This procedure allows the determination of the ion energy loss in the target. As a result, 11.4 MeV/u calcium beam energy losses in aerogel and aluminum targets have been determined. The experimental results are summarized in Table I. Experimental data on the stopping power for fast ions are traditionally compared with the values predicted by the publicly available SRIM code [38].

We also present such a comparison in Table I. One can see that our experimental results on the Ca ion energy loss in Al targets are in good agreement with SRIM2003 values.

For the analysis of charge state distribution after interaction with the investigated target, the beam burst is deflected in the $B = 1-1.8$ T magnetic field of a dipole magnet. The ions are split according to their charge-to-mass ratio Q/m and energy. The ion impacts were detected by a plastic scintillator (1 mm thick), viewed by a camera which produces intensified images on a charge coupled device (CCD). The background picture of the foreign lighting and CCD noise was registered and subtracted for each image. Afterwards, the images were projected along the direction of the dispersion. Since the beam energy after the target is known from
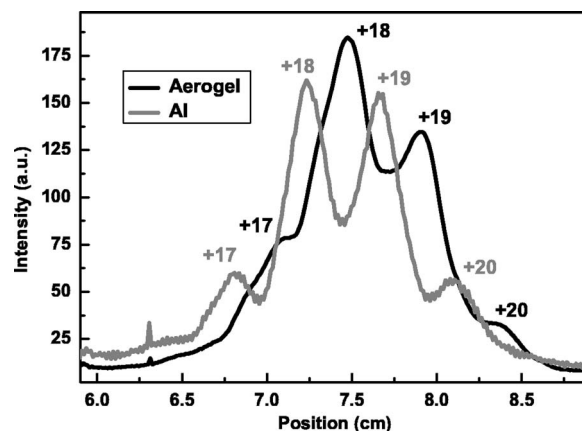
the TOF measurements, the charge state distribution of the ion beam can be determined.

Figure 4 shows the charge state distribution of the Ca ion beam with initial energy of 11.4 MeV/u after penetration of the 50-μm-thick Al foil and the aerogel target of approximately the same linear density. The measured ion beam energies after the aluminum target are 8.3 MeV/u, and after the piece of aerogel 8.06 MeV/u.

The curves are shifted along the x axis due to the difference in the final energy of the ion beam. The averaged Ca ion charge measured after the Al target is $Z_{av} = 18.5$; the averaged ion charge measured after the aerogel target is $Z_{av} = 18.2$ with the experimental accuracy of 1–2%. These results allow suggesting that at our experimental conditions the pore of 30–50 nm size does not seriously influence the ion stopping processes.

B. *K*-shell radiation of Si target atoms

In fast ion-atom collisions, the production of a *K*-shell vacancy in the target atom can be accompanied by the production of one or more *L*-, and *M*-shells vacancies. This process is of high probability. The *K*-shell x-rays from decays of excited states with different *L*-shell vacancies are shifted to higher energies than those from a *K*-vacancy state with a completed *L* shell. A spectral resolution of the detector better than $\lambda/\delta\lambda = 1000$ is required to resolve this group of satellites. In experiments on the interaction of ^{48}Ca ions with quartz and silica gel targets, *K*-shell radiation of Si target atoms was measured along the ion beam trajectory. The ion beam was fully stopped in both targets: a 1-mm-thick quartz plate with a density of 2.23 g/cm^3 and a 25-mm-thick piece of SiO$_2$ gel with a mean density of 0.04 g/cm^3. Figure 5 shows Si $K\alpha$ spectra of quartz and silica aerogel irradiated by a ^{48}Ca ion beam with the initial energy of 11.4 MeV/u. The stopping length of Ca ions in aerogel reached 9 mm. The corresponding length of the spectral lines increased dramatically as well. In contrast to the quartz target spectrum, one can resolve the dynamics of the $K\alpha$ satellite intensity distri-
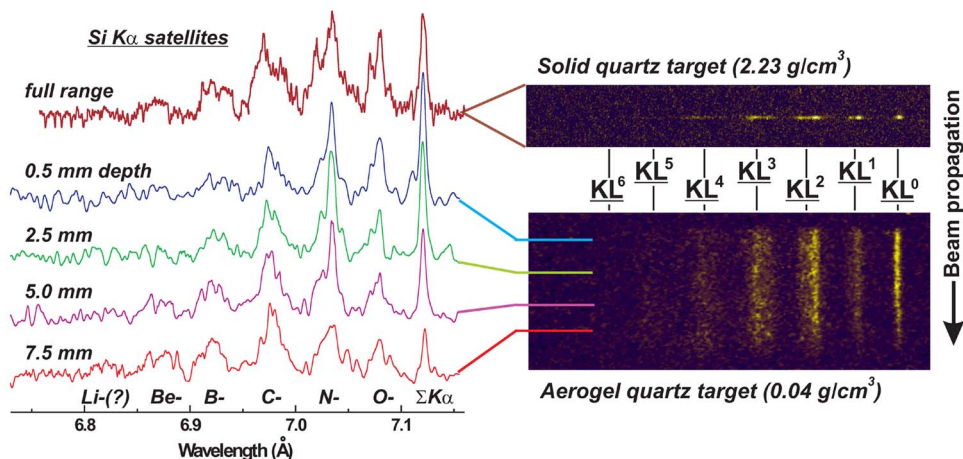
FIG. 5. (Color online) Si target $K\alpha$ spectra produced due to irradiation of 2.23 g/cm^3 solid quartz and 0.04 g/cm^{3}SiO$_2$-aerogel targets by 11.4 MeV/u ^{48}Ca ions under the same experimental conditions.

bution along the ion beam trajectory due to the change of the energy and the charge of Ca projectile ions.

Both target spectra show radiative transitions in Si ions having one K-shell vacancy and one or more L-shell vacancies. This transitions are usually designated as $K\alpha L^n$, where n is the amount of L-shell vacancies [28]. In the Si target K-shell spectrum, we can observe the radiative transitions in highly ionized Si ions having up to 5 vacancies in the L shell. The line KL^0 accumulates the radiative transitions in Si ions with a filled L shell and different amounts of M-shell vacancies which are not resolved. The spectral and spatial resolutions in our experiments are $\lambda/\delta\lambda = 3000$ and 50–70 μm, respectively.

In the Si K-shell target spectrum resolved along the ion beam path, we can observe the satellite intensity redistribution. At the end of the ion path, intensities of the satellite groups having many L-shell vacancies KL^3 and KL^4 are increasing and even KL^5 satellites appear instead of the disappeared KL^1 one. This correlates to the fact that the L-shell ionization probability increases at lower ion energies.

$K\alpha$ x-ray satellites induced by the ion-atom collisions in solid targets have been intensively studied [28–33]. It has been demonstrated [28–30], that the distribution of L-shell vacancies which produces the $K\alpha L^n$ satellites can be fitted by a binomial distribution for the probability of L-shell vacancy production at small impact parameters. The response of the K-shell target spectra to the ion beam parameters such as the ion energy and the ion charge state was in the focus of the

experimental researches in the 1970s and 1980s [31–33].

It was shown that there is a strong dependence of the K-shell projectile and target spectra on the ion charge state and velocity. This opens perspectives to use spatially resolved target spectra for the stopping process analysis. Kaufmann [34] showed using Si solid and SiH$_4$ gaseous targets irradiated by Cl ion beam the dramatic dependence of the K-shell spectra on the state of stopping media. This fact can be used by observation of phase transitions in matter irradiated by intense energetic ion beams in the warm dense matter production scenario.

C. Ca projectile K-shell radiation

In experiments on the interaction of heavy ions with low-density silica aerogels, the ion radiation dynamics along the stopping path was resolved for the first time. Figure 6 shows spatially resolved $K\alpha$ radiation of 11.4 MeV/u Ca ions being slowed down in the 25-mm-thick aerogel sample of 0.04 g/cm^3 mean density. Projectile K-shell radiation was registered over 8 mm of the ion stopping path.

K-shell spectra of energetic ions recorded with a high spectral and spatial resolution reveal very interesting features.

(a) We observe intense long-lasting radiation of Ly$_\alpha$ and He$_\alpha$ lines over 70–80 % of the ion stopping length. At the middle of the stopping length (at 3–5 mm of the penetration depth, Y axis in Fig. 5), the $K\alpha$ satellites corresponding to
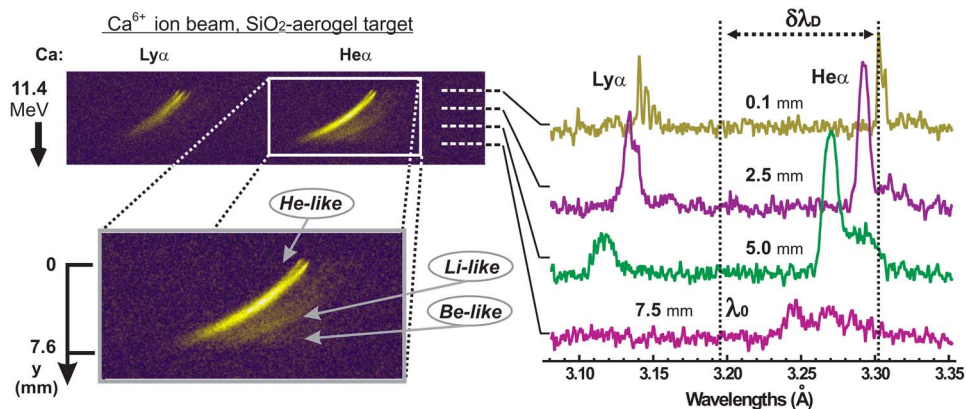

FIG. 6. (Color online) Radiation dynamics of Ca ions with the initial energy $E_0 = 11.4$ MeV/u slowing down in silica aerogel ($\rho = 0.04$ g/cm^3). Y axis represents the ion penetration depth.
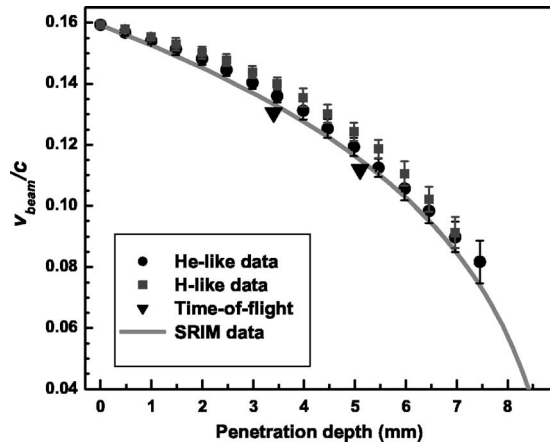
FIG. 7. Ca ion velocity normalized to the light speed versus penetration depth in SiO_2 with a mean density of 0.04 g/cm³. Measured x-ray spectroscopic (squares and circles) and time-of-flight (triangles) data are compared with SRIM calculation.

the radiative transitions in Li- and Be-like electronic systems of Ca can be recorded. The low ionic charge states appear due to the process of capture of bound target electrons by the projectile ion at lower energies.

(b) In contrast to the target K-shell spectra having vertical lines (see Fig. 5), projectile lines registered with a spatial resolution are tilted demonstrating the reduction of the line Doppler shift due to the ion deceleration in stopping media. This effect was discovered in experiments on the interaction of 5.9 MeV/u Ni ions with 0.1 g/cm³ SiO_2-aerogel targets [25]. Then, it was confirmed and analyzed in details in experiments on the irradiation of 0.1 and 0.15 g/cm³ aerogels by Ar, Ca, and Ti fast ions [36,37]. The ion enters the target surface ($y=0$ mm, Y axis, Fig. 6) having a maximum velocity, therefore the wavelength shift $\delta\lambda_D$ from the position λ_0 of the ion in rest due to the Doppler effect is maximum. By deeper penetration into the target, the projectile ion looses its energy and the line Doppler shift is decreasing continuously.

V. ANALYSIS OF THE ION VELOCITY DYNAMICS

The Doppler effect observed on the projectile K-shell spectra was used for calculations of the ion velocity dynamics inside the interaction volume. The following relativistic equation for the line Doppler shift was used:

$$\lambda_D = \lambda_0 \left(\frac{1}{\sqrt{1-(\nu/c)^2}} + \frac{(\nu/c)\sin\varphi}{\sqrt{1-(\nu/c)^2}} \right),$$

where λ_D is the measured wavelength, λ_0 is the wavelength of a radiative transition in the ion at rest, ν is the projectile ion velocity, c is the speed of light, and φ is the angle to the beam axis.

From the space-resolved analysis of the relative Doppler line shift $\delta\lambda_D$, the experimental dependence of the projectile velocity ν on the ion penetration depth in target material was found (Fig. 7). In our calculations we started with the assumption that the velocity of ions at the beginning of Ly_α and He_α line emission ν_{beam} corresponds to the initial ion

beam energy. In fact, the ionization length l_{ion} of ions entering the target surface can be estimated as $l_{ion}=1/\sigma_{ion}n_e$; here $\sigma_{ion}(cm^2)$ is the ionization cross section and n_t (at./cm³) is the target density. Using the results of the calculations in Fig. 1, we can estimate the length at which Ca^{6+} will be ionized to Ca^{19+} as 10–20 μm. This is below our spatial resolution. The accuracy of ion velocity measurements is determined by spectral resolution, varying from 2% to 15% due to the decrease of K-shell ionization cross sections and broadening of the ion beam energy profile in media. The experimental data were compared to the numerical calculations using the open semiempirical SRIM code and time-of-flight measurements (see Fig. 7). Measurements were made after the Ca ion beam emerged from a 3.4-mm-thick piece of a 0.04 g/cm³ and an 8.3-mm-thick piece of 0.023 g/cm³ aerogel with linear densities of 13.6 and 19.3 mg/cm², respectively. The last measurement could be described as the same for the sample with 0.04 g/cm³ density with corresponding linear density and the thickness of 4.7 mm. From the comparison, the difference of energy values obtained by two experimental methods is within 7%.

In experiments with the Ca ion beam, the final projectile energy which has been measured by mean of the DSR method using Ly_α and He_α characteristic lines is 2.8–3 MeV/u. From Fig. 1 one can see that Ca projectile energies below 1–2 MeV/u cannot be analyzed due to low-K-shell ionization cross sections. Nevertheless, this can be possible for low Z projectile ions such as Ne or Mg having low K-shell electron binding energy.

VI. ANALYSIS OF THE PROJECTILE CHARGE STATE DYNAMICS

The dynamics of Ca projectile charge states along the beam trajectory (Fig. 6) shows the increase of the $K\alpha$-satellite intensities corresponding to the radiation of Ca^{17+} and Ca^{16+} ions due to the capture of the target bound electrons by projectile ions at lower energies.

Qualitatively the behavior of the ion charge with the penetration depth (ion energy) is in an agreement with the Ca ion charge state distribution analyzed after the ion beam emerges from an 8.3-mm-thick piece of 0.023 g/cm³ aerogel with the corresponding linear density of 19 mg/cm² (see Fig. 8). The measured fractions of the Ca charge states are Ca^{20+}, 2.8%; Ca^{19+}, 16.7%; Ca^{18+}, 44.7%; Ca^{17+}, 28%; Ca^{16+}, 6.7%; Ca^{15+}, 1.1%.

Generally, $K\alpha$-satellite intensity is proportional to the population of the projectile ion excited state $1s2pml^k$ which gives rise to these radiative transitions. For Ca^{19+} this is a $2p$ state, for Ca^{18+} a $1s2p(^1P_1)$ state. The $2p$ state can be populated by three different mechanisms: due to the bound electron capture of target electrons by Ca^{20+}, due to the excitation of the projectile bound electron from the ground state in Ca^{19+} ($1s$-$2p$), and by the ionization of $1s$ electrons from an excited state $1s2p$ of Ca^{18+}. The role of each of these mechanisms depends on the ion energy and charge state distribution. The same is valid for $1s2p$ state of Ca^{18+}. Therefore, there are at least three projectile charge states involved in the analysis of the Ly_α and He_α radiative transitions. $K\alpha$ transi-
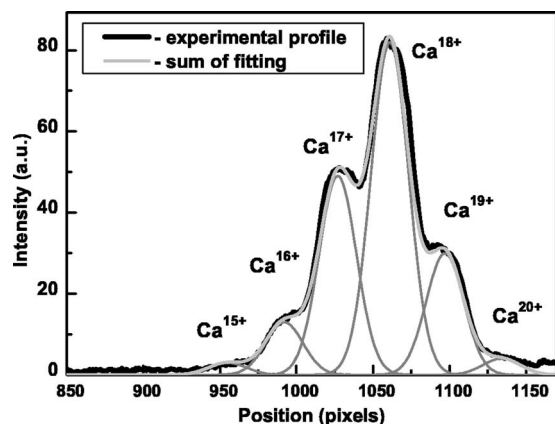
FIG. 8. Charge state distribution of Ca ions with initial energy of 11.4 MeV/u after emerging from the 0.023 g/cm^3 aerogel sample with a linear density of 19 mg/cm^2. Data were obtained by the method of magnet spectroscopy with magnet field value of $B=1.63$ T. The measured ion beam energy after the target $E=6.54$ MeV/u.

tions in Ca^{17+} and lower-Z charges arise from autoionization states $1s2s^m2p^k$ ($m=0$, 1, 2, $k=0,…$, 6 depending on the ion charge and electronic configuration). These electronic states are produced due to the K-shell ionization of the projectile ground and excited states $1s^22s^m2p^k$. These configurations can decay not only via radiation but as well due to the Auger effect; therefore their line intensities depend as well on the fluorescence factor $\Gamma_r/(\Sigma\Gamma_r+\Gamma_A)$, where Γ_r is the radiative decay probability, and Γ_A is the Auger decay probability. According to the calculated values of fluorescence factors [37], the radiative transitions from excited electronic configurations with $m=0$, 1 give the main input in to the K-shell spectrum. Autoionizing levels produced due to K-shell ionization of the projectile ground states with $1s^22s^22p^k$ ($m=2$) have mostly low radiative transition probabilities.

The quantitative analyzes of the ion charge state distribution and the ion effective charge in stopping media using K-shell satellite intensities demands detailed calculations of the projectile excited and ground state population kinetics caused by collision and noncollision processes. The advan-

tage provided by this experimental method is that for calculations of the rates of collision processes we can use the measured dependence of the projectile velocity on the ion penetration depth. The process of the spectra simulations is now in work. It will allow reconstructing the dynamics of the projectile bound electron structure and the ion charge state distribution along the projectile stopping path.

VII. CONCLUSION

Application of low-density aerogels as stopping media provides a stretching of the ion stopping length in solid matter and resolves the K-shell radiation dynamics of projectiles and target atoms. Ion beam energy loss and charge state measurements allow concluding that a nanometer porous aerogel structure has no significant influence on the ion stopping process.

The projectile ion velocity dynamics was measured spectroscopically using the method of Doppler shift reduction. Experimental results are in good agreement with calculated data and time-of-flight measurements.

The dynamics of the ion charge state distribution which can be observed in the projectile K-shell spectra and those measured by means of the dipole magnet are in qualitative agreement. The work on the projectile K-shell spectra simulation is in process. Experimentally measured dependence of the velocity dynamics versus the ion penetration depth will be used for the calculations of the ion-atom collision cross sections.

K-shell projectile and target radiation is a promising instrument for the complete analysis of the ion stopping process allowing measurements of the projectile ion charge and velocity dynamics directly from the region of the ion-beam–target interaction.

[1] S. P. Ahlen, Rev. Mod. Phys. **52**, 121 (1980).
[2] L. C. Northcliffe, Annu. Rev. Nucl. Sci. **13**, 67 (1963).
[3] P. Sigmund and A. Schinner, Nucl. Instrum. Methods Phys. Res. B **174**, 535 (2001).
[4] H. D. Betz, Rev. Mod. Phys. **44**, 465 (1972).
[5] L. C. Northcliffe and R. F. Schilling, Nucl. Data, Sect. A **7**, 233 (1970).
[6] J. F. Ziegler, J. Appl. Phys. **85**, 1249 (1999).
[7] V. S. Nikolaev, I. S. Dmitriev, Phys. Lett. A **88**, 26 (1982).
[8] N. O. Lassen, K. Dan. Vidensk. Selsk. Mat. Fys. Medd. **26**, 5 (1951).
[9] H. Geissel, Y. Laichter, W. F. W. Schneider, and P. Ambruster, Phys. Lett. **88A**, 26 (1982).
[10] D. H. H. Hoffmann, *et al.*, Laser Part. Beams **23**, 55 (2005).
[11] W. F. Henning, Nucl. Instrum. Methods Phys. Res. B **214**, 211 (2004).
[12] D. G. Koshkarev, Laser Part. Beams **20**, 595 (2002).
[13] N. A. Tahir *et al.*, Phys. Rev. ST Accel. Beams **6**, 020101 (2003).
[14] R. Bimbot *et al.*, Nucl. Instrum. Methods Phys. Res. B **44**, 1 (1989).
[15] D. H. H. Hoffmann *et al.*, Phys. Rev. A **42**, 2313 (1990).
[16] K. G. Dietrich *et al.*, Phys. Rev. Lett. **69**, 3623 (1992).
[17] N. Bohr and J. Linhard, K. Dan. Vidensk. Selsk. Mat. Fys.

Medd. **28**, 1 (1954).

[18] H. D. Betz and L. Grodzins, Phys. Rev. Lett. **25**, 211 (1970).

[19] R. Anholt, Phys. Rev. A **31**, 3579 (1985).

[20] G. Maynard *et al.*, Nucl. Instrum. Methods Phys. Res. B **195**, 188 (2002).

[21] G. Schiwietz and P. L. Grande, Nucl. Instrum. Methods Phys. Res. B **175**, 125 (2001).

[22] V. P. Shevelko, I. Yu. Tolstikhina, and Th. Stölker, Nucl. Instrum. Methods Phys. Res. B **184**, 295 (2001).

[23] A Ya. Faenov *et al.*, Phys. Scr. **50**, 333 (1994).

[24] B. L. Henke and P. A. Jaanimagi, Rev. Sci. Instrum. **56**, 1537 (1985).

[25] O. N. Rosmej *et al.*, Nucl. Instrum. Methods Phys. Res. A **495**, 2 (2002).

[26] N. G. Borisenko and Ya. A. Merkuliev, Proc. (Tr.) P.N. Lebedev Phys. Inst. **221** (1996).

[27] B. A. Demidov *et al.*, Zh. Tekh. Fiz. **43**, 1239 (1998).

[28] Y. Awaya, T. Kambara, and Y. Kanai, Int. J. Mass. Spectrom. **192**, 49 (1999).

[29] C. Schmiedekamp *et al.*, Phys. Rev. A **18**, 1892 (1978).

[30] C. L. Cocke, Phys. Rev. A **20**, 749 (1979).

[31] J. R. Mowat, I. A. Sellin, D. G. Pegg, and R. S. Peterson, Phys. Rev. Lett. **30**, 1289 (1973).

[32] J. R. Macdonald, M. D. Brown, S. J. Czuchelewski, and L. M. Winters, Phys. Rev. A **14**, 1997 (1976).

[33] H. F. Beyer, R. Mann, F. Folkmann, and P. H. Mokler, J. Phys. B **15**, 3853 (1982).

[34] R. L. Kaufmann, K. A. Jamison, T. J. Gray, and P. Richard, Phys. Rev. Lett. **36**, 1074 (1976).

[35] O. N. Rosmej *et al.*, Rev. Sci. Instrum. **74**, 5039 (2003).

[36] O. N. Rosmej *et al.*, Laser Part. Beams **23**, 79 (2005).

[37] U. I. Safronova and T. G. Lisina, At. Data Nucl. Data Tables **24**, 50 (1979).

[38] www.SRIM.org